Molecular dynamics modeling of mechanical loss in amorphous tantala and titania-doped tantala

Jonathan P. Trinastic, Rashid Hamdan, Chris Billman, and Hai-Ping Cheng

Molecular dynamics modeling of mechanical loss in amorphous tantala and titania-doped tantala

Jonathan P. Trinastic,[1] Rashid Hamdan,[1] Chris Billman,[1] and Hai-Ping Cheng*[1]

[1]*Department of Physics and Quantum Theory Project,*

University of Florida, Gainesville, Florida, 32611, USA

(Dated: January 11, 2016)

Abstract

The mechanical loss (Q^{-1}) intrinsic to amorphous oxides is the limiting factor for sensitive, high-precision gravitational wave detectors and optical devices. Recent experimental work suggests that doping amorphous tantala with titania reduces Q^{-1}, however the physical processes underlying this reduction are unknown. Here we calculate Q^{-1} for pure and titania-doped tantala using numerical methods combined with molecular dynamics simulations that have atomic levels of resolution. Our results match experimental trends that titania doping decreases the magnitude of the low-temperature loss peak characteristic of these materials, with 62% titanium cation doping minimizing Q^{-1} at low temperature. We provide a microscopic explanation for this reduced loss by examining how doping affects the potential energy landscape, strain coupling constant, relaxation time, and other properties of the amorphous materials within the framework of the double well potential model. Analyzing configurational changes provides the first atomic description of the transitions driving mechanical loss at various temperatures in these oxides. These results identify the important parameters contributing to Q^{-1} that are most affected by doping and provide guidance for how to screen for optimal doping combinations to minimize loss in other materials.

PACS numbers: 63.50.Lm,62.20.D,62.20.Qp

I. INTRODUCTION

High-precision measurement devices such as optical clocks[1] and interferometers[2] rely on mirror coatings with low thermal noise to achieve large signal-to-noise ratios. In particular, the Laser Interferometer Gravitational Observatory (LIGO) aims to detect gravitational waves by measuring the displacement of suspended mirrors with coatings made of amorphous oxides. The thermal noise intrinsic to the coating limits the detector sensitivity between 30-500 Hz, which coincides with the most sensitive band of the interferometer[2,3]. Shot and seismic noise dominate contibutions to the total noise above and below this frequency range, respectively[3].

Many attempts are underway to minimize thermal noise within this sensitive frequency range[4–9]. Experiments measure the mechanical loss (Q^{-1}, also known as internal friction) of amorphous oxides, which directly relates to thermal noise via the fluctuation-dissipation theorem[10,11]. To date, mirror coatings made of alternating layers of amorphous silica (SiO_2) and tantala (Ta_2O_5) have resulted in the lowest values of mechanical loss, with tantala acting as the dominant source of noise[6–8]. Recent research suggests that doping Ta_2O_5 with titania (TiO_2) can reduce the loss by 20-40% with 14-25% Ti cation substitution[6,9] while also retaining the optical absorption requirements for the interferometer[6]. Understanding why TiO_2 decreases loss will provide insight into how to minimize noise to a greater degree in future coatings.

Atomic modeling of such systems plays an important role in elucidating the physical processes underlying Q^{-1} and guiding choices of optimal doping combinations. Internal friction arises from energy dissipation from the perturbing source (e.g., light or sound waves) into the internal degrees of freedom of the coating. In amorphous solids, the lack of long-range order allows for low-energy excitations involving small groups of atoms that serve as the fundamental source of this energy dissipation. These excitations can be modeled as a particle transitioning between two level-systems (TLS) within the solid's potential energy landscape (PEL)[12,13], giving amorphous materials many of their thermal, elastic, and dielectric properties[14]. Below several Kelvin, transitions between TLSs occur via quantum tunneling[15]. At higher temperatures, of primary interest in LIGO, the same PEL determines Q^{-1} but transitions are mainly due to thermally activated processes[16].

The success of the TLS model has thus far been phenomenological and the microscopic

origin of TLS transitions has remained elusive[17]. However, recently developed computational techniques allow for the simulation of atomic movement inside amorphous materials over a timescale during which these transitions can be observed[18–20]. Such techniques provide a method to understand the origin of transitions at an atomic level and to predict material combinations that minimize mechanical loss.

In this paper, we investigate the internal friction due to thermally activated processes in pure and titania-doped tantala using our recently developed computational method to search for TLSs in amorphous materials[21]. Our results match experimental trends showing a decrease in Q^{-1} with TiO_2 doping and find that 62% Ti cation doping minimizes the mechanical loss at low temperature. We explain this pattern by examining the effect of doping on the potential energy landscape and the TLS properties, including the coupling to strain, Young's modulus, and relaxation time. We also connect transitions with different barrier heights to particular types of cation and anion motion, giving the first atomic description of the motion causing loss at low and room temperatures in these materials. The calculations provide important information about the origin of microscopic excitations that have not yet been explored in amorphous tantala and titania as well as the physical processes that govern how doping affects Q^{-1}.

The rest of the paper is organized as follows. Section II.A introduces the theory of TLSs. Sections II.B-D describes the computational methods implemented to search for TLSs and calculate the internal friction. In Section III, we discuss our results regarding how TiO_2 doping influences the internal friction and explore the underlying potential energy landscape and physical parameters to understand why TiO_2 reduces loss. Finally, we discuss general conclusions in Section IV.

II.   THEORY AND METHODS

A.   Theory of Two-Level Systems and Internal Friction

The PEL of amorphous materials is rugged such that transitions between local energy minima are possible by simple rearrangements of atomic subsets. This landscape allows an amorphous solid to be modeled as a particle that moves between double wells separated by

an energy barrier, where each well corresponds to a different configuration of the same set of atoms. Such transitions from one well to another are possible via coupling to external strain, e.g. from light or sound waves, and thermal motion. The atoms and PEL corresponding to such a transition form a TLS. Mathematically, a TLS is characterized by the energy asymmetry between the two wells (Δ), the height of the energy barrier separating them (V), and the configurational distance between them (d) (Figure 1)[12,13,21].
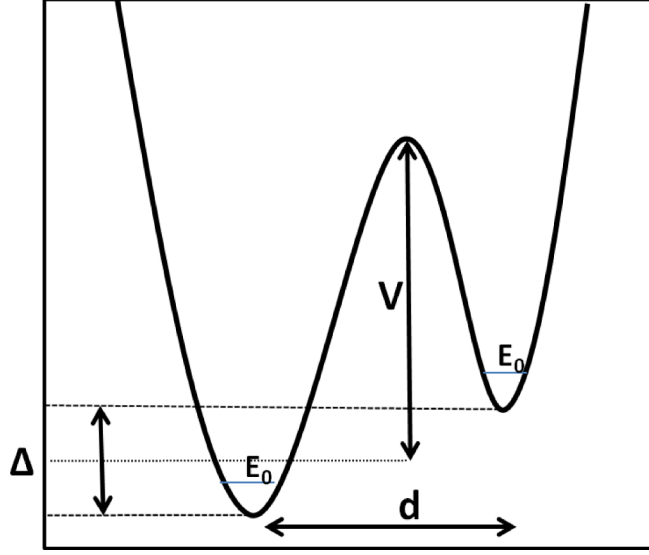

FIG. 1. Sketch of a two-level system (TLS) modeling the potential energy landscape of amorphous solids. Δ is the energy asymmetry between the two minima, V is the barrier height, d is the configurational distance between the two wells, and E_0 is the ground state energy.

The internal friction ($Q_{l/t}^{-1}(\omega, T)$) measures the energy dissipated through an amorphous solid due to longitudinal (l) or transverse (t) waves. At temperatures above 5 K, thermal transitions dominate over quantum tunneling and $Q_{l/t}^{-1}(\omega, T)$ can be expressed as[16]:

$$Q_{l/t}^{-1}(\omega, T) = \frac{\gamma_{l/t}^2}{E_{l/t} k_B T} \int_0^\infty \int_0^\infty \frac{\omega\tau}{1 + \omega^2\tau^2} \text{sech}^2 \left(\frac{\Delta}{2k_B T} \right) f(\Delta)g(V)d\Delta dV, \qquad (1)$$

where τ is the thermally activated relaxation time, $\gamma_{l/t}$ is the longitudinal (l) or transverse (t) strain coupling constant (also known as the deformation potential), $E_{l/t}$ is the elastic modulus of interest, and ω is the observation frequency of the perturbing wave. The TLS barrier height and asymmetry distributions are $g(V)$ and $f(\Delta)$, respectively, which are calculated using methods described in the next section. The barrier distribution has units of [energy]$^{-1}$ and is normalized to one, whereas $f(\Delta)$ has units of [energy]$^{-1}$[volume]$^{-1}$ and

4

is normalized such that its integration over energy asymmetry (Δ) gives the TLS density per volume (N).

In most experiments, the internal friction is measured using a cantilever with an applied force normal to the amorphous solid's surface[22], which mainly causes longitudinal disturbances in the material. Therefore, here we calculate the internal friction using the longitudinal coupling constant (γ_l) and the Young's modulus ($E_l = Y$) to best compare witih experimental results ($Q^{-1} = Q_l^{-1}$).

The relaxation time (τ) for thermally activated transitions is given by an Arrhenius expression[16]:

$$\tau^{-1} = \tau_0^{-1} \cosh \left[\frac{\Delta}{2k_B T} \right] \exp^{-V/k_B T}, \tag{2}$$

where τ_0^{-1} is known as the attempt frequency, k_B is Boltzmann's constant, and T is temperature. The attempt frequency is calculated from the normal modes at the bottom of the well (ν_i^0) and at the saddle or transition point (ν_i^t), i.e. the vibrational frequency in the direction from the potential well to the saddle point[23]:

$$\tau_0^{-1} = \frac{\prod_{i=1}^{3N} \nu_i^0}{\prod_{i=1}^{3N-1} \nu_i^t} \exp^{S/k_B} . \tag{3}$$

Because of the exponential dependence of τ on V, the distribution of relaxation times in an amorphous solid mainly depends on the barrier height distribution. Thus, we assume that variations in τ_0 have little effect on the distribution of τ and approximate τ_0 as an average calculated across all TLSs.

The exponential term in Equation 3 is necessary because the free energy ($F = V - TS$) is used to derive the Arrhenius expression, where S is the entropy of the transition state at the saddle point[24]. This term describes the number of minima connected to a single transition state. Previous work has found that numerical results best match experimental internal friction data for silica when $S/k_B = ln4$[21,25], and we use the same value here to study tantala and titania-doped tantala.

The strain coupling constant (γ) describes the variation of the TLS asymmetry due to the strain induced by the perturbing wave. In general, γ is a 6×6 tensor, however in isotropic solids the longitudinal (transverse) components are expected to be equal. This allows for independent longitudinal (γ_l) and transverse (γ_t) coupling constants to be calculated:

$$\gamma_{l(t)} = \frac{1}{2} \frac{\partial \Delta}{\partial u_{l(t)}}, \tag{4}$$

where $u_{l(t)}$ are the longitudinal (transverse) components of the strain matrix. Here we report both longitudinal and transverse components but only use the longitudinal coupling constant to calculate the internal friction using Equation 1.

The Young's modulus (Y) measures the stiffness of the amorphous solid and is calculated using elastic moduli:

$$Y = \frac{9BG}{3B + G},$$ (5)

where B is the bulk modulus and G is the shear modulus. The moduli are calculated using elastic constants as described in our previous work.[21,26,27]

B. Classical Force Field Parameters

We have modeled amorphous, TiO_2-doped Ta_2O_5 samples and calculated their corresponding $Q^{-1}(\omega, T)$ using classical molecular dynamics simulations and techniques implemented in the DLPOLY 2.20 software package[28]. We describe atomic interactions using a classical force field that describes Pauli repulsion and van der Waals interactions using the BKS potential[29] as well as partially covalent anion-cation interactions using a Morse potential. The potential energy due to the interaction between atoms i and j is:

$$\Phi_{ij} = q_i q_j / r_{ij} + A_{ij} \exp(-r_{ij}/\rho_{ij}) - C_{ij}/r_{ij}^6$$
$$+ D_{ij}(1 - \exp(-a_{ij}(r_{ij} - b_{ij})))^2,$$ (6)

where r_{ij} is the distance between atoms i and j. The first term represents the Coulomb interaction, the second represents Pauli repulsion, and the third represents the van der Waals attraction. These three terms comprise the original BKS potential used to model amorphous silica.[29] The last term is the Morse potential, added to better model the partially covalent interaction between anions and cations in these oxides.[27] Only electrostatic forces describe cation-cation interactions, which allows for mixing of different oxides without adjusting the force field parameters.

We have fit the potential parameters A_{ij}, ρ_{ij}, D_{ij}, a_{ij}, and b_{ij} to reproduce radial distribution functions and elastic constants of the amorphous solids studied here. Since the amorphous structure and elastic moduli are the key quantities affecting the internal friction (through the TLS distribution, Young's modulus, and coupling constant), these interatomic potentials should be adequate for exploring Q^{-1} in tantala and titania. Details about the

6

fitting procedure and results can be found in our previous work.[27] In summary, this two-body potential balances accurate modeling of structural and mechanical properties with computational efficiency in order to effectively search the potential energy landscape for thousands of TLSs.

Amorphous TiO_2 can exist in two forms with different coordination numbers and elastic properties arising from various processing methods. Ion-beam sputtering result in a sample with mostly six-coordinated Ti atoms and a larger Young's modulus between 147 and 169 GPa[30,31]. Other methods such as sol-gel or reactive evaporation provide softer, four-coordinated samples with a Young's modulus of 64 GPa[30,32]. Since most amorphous oxides used for optical coatings and in gravitational wave detection use sputtering techniques[2], we use potential parameters that generate the stiffer, six-coordinated amorphous TiO_2 sample to dope Ta_2O_5 to better compare to experimental results.

C.   Amorphous Samples and Annealing Procedures

To understand how TiO_2 doping affects Q^{-1}, we dope Ta_2O_5 incrementally by replacing roughly 12.5% of Ta with Ti cations while keeping the total number of atoms constant (1008 total atoms). To match exact experimental doping percents, we slightly adjust the doping amounts to end with eight different samples: pure Ta_2O_5, 14% Ti, 25% Ti, 41% Ti, 53% Ti, 62% Ti, 76% Ti, and pure TiO_2. For example, the 25% Ti-doped Ta_2O_5 consists of 222 Ta, 77 Ti, and 709 O atoms. Such small increments will allow for the observation of systematic trends in parameters to identify physical mechanisms that explain the effect of Ti doping. Each simulation box is cubic with lengths between 19 and 22 Å, which is large enough to capture the long-range disorder of the amorphous materials.

To produce the annealed amorphous samples, the extended Ta_2O_5 crystal structure is equilibrated at 300K with an NVT ensemble and then heated to 6000K over 160 ps using an NPT ensemble. At 6000K, the sample is equilibrated again with an NVT ensemble for 50 ps and then quenched to 300K over 160 ps with an NPT ensemble. The sample is finally equilibrated again for 50 ps and then energy-minimized using an NVE (microcanonical) ensemble. Radial distribution functions are examined to confirm the amorphous nature of the sample after quenching from high temperature. We have used a 1 femtosecond time step for all simulations.

To obtain doped samples, we randomly replace Ta atoms in the amorphous sample with the desired number of Ti atoms and complete the same procedure above to arrive at a newly annealed and doped sample.

D.   Barrier Search and Internal Friction Calculation

To find two-level systems, we bring an annealed configuration to a running temperature ($T_{run} \approx 1000$ K) and collect an MD trajectory with 500,000 time steps using an NVT ensemble and a 1 femtosecond time step. Within each trajectory, the interval bisection method[20] searches for transitions from one local minima to another after a specified number of time steps. Once adjacent local minima are found, the nonlocal ridge method[20] determines the saddle point between them to calculate the barrier height. A pair of minima connected by a first-order saddle point forms a TLS. Following the system through the MD trajectory and employing this procedure results in a collection of TLSs and a distribution of asymmetries ($f(\Delta)$) and barriers ($g(V)$) used to calculate Q^{-1} (Equation 1).

To ensure proper sampling of the PEL, we have searched for two-level systems using at least five distinctly annealed samples for each doping amount. The search for TLSs is continued until the barrier and asymmetry distributions do not significantly change with the addition of more data. We find that roughly 1000 TLSs are required to reach such convergence. In addition, we have only included TLSs with $\Delta < 0.1$ eV because larger values correspond to highly defected states not seen experimentally in other amorphous solids, such as silica[20,33].

We implement a separate search method to the TLS density (N) such that $f(\Delta)$ can be properly normalized to N. In this case, a single local minimum is chosen as the starting point for an MD trajectory. Once a connected minimum is found along the trajectory, the system is returned to the configuration of the first minimum and the search is resumed with randomized starting velocities. By continually repeating this procedure, we find the total number of minima connected to the original basin. The density N is the number of connected minima, averaged across many different starting configurations, divided by the volume of the simulation cell. We find that N is fairly consistent across all levels of doping, varying as a function of Ti concentration only within the standard error of their distributions. Therefore, we have calculated the average TLS density across all doping samples, $N = 4.5$, and used

8

this value as a constant input for all calculations of the internal friction.

We determine the coupling constant ($\gamma_{l/t}$) and average relaxation time (τ_0) using the set of TLSs that give a converged distribution of asymmetries and barrier heights. For each pair of minima in a given TLS, we apply increasing amounts of strain (0 to 0.5 percent) to compress and stretch the cell and then allow the atoms to relax to their new energy minimum for each level of strain. The six components of the coupling constant (γ_{ij}) are then calculated as the slope of the asymmetry as a function of the strain (u_{ij}) applied to the cell. The arithmetic averages of γ_l and γ_t (Equation 4) are calculated across all TLSs for a given system. To determine τ_0, the Hessian matrix is calculated for the configuration at each minima and the saddle point corresponding to each TLS. The eigenvalues of the Hessian matrix are input into Equation 3 to calculate the relaxation time for a given TLS. τ_0 is then the average of these values across all TLSs.

Finally, we calculate the Young's modulus (Y) by determining the elastic constants of the amorphous sample and entering them into Equation 5. We have calculated elastic constants using methods described in our previous work[21,26,27]. We calculate Y as an average across ten different annealed samples of the same material.

Using the distributions $f(\Delta)$ and $g(V)$, along with the averaged values of γ_l, τ_0, and Y, we solve Equation 1 numerically to calculate Q_l^{-1} for each amorphous system. A more detailed description of methods described above can be found in our previous work[21].

III. RESULTS AND DISCUSSION

A. Internal Friction

We first discuss how Ti doping of Ta_2O_5 affects the internal friction of the amorphous samples. Figures 2(a)-(b) plot $Q^{-1}(T)$ of pure and TiO_2-doped Ta_2O_5 with an observation frequency of $\omega = 1$ kHz, matching the same magnitude used in recent experimental measurements[9]. As seen in Figure 2(a), pure Ta_2O_5 exhibits a low-temperature peak of $Q^{-1}(T_{peak}) = 27.80 \times 10^{-4}$ at 30 K, closely matching the characteristic peak seen in experiment near 20 K in Ta_2O_5[9] as well as in amorphous silica[21,25]. The magnitude of the calculated low-temperature peak is in good agreement with experiment, within the same order of magnitude but a factor of 2.5 larger than the experimental value of $Q_{exp}^{-1}(T_{peak}) =$
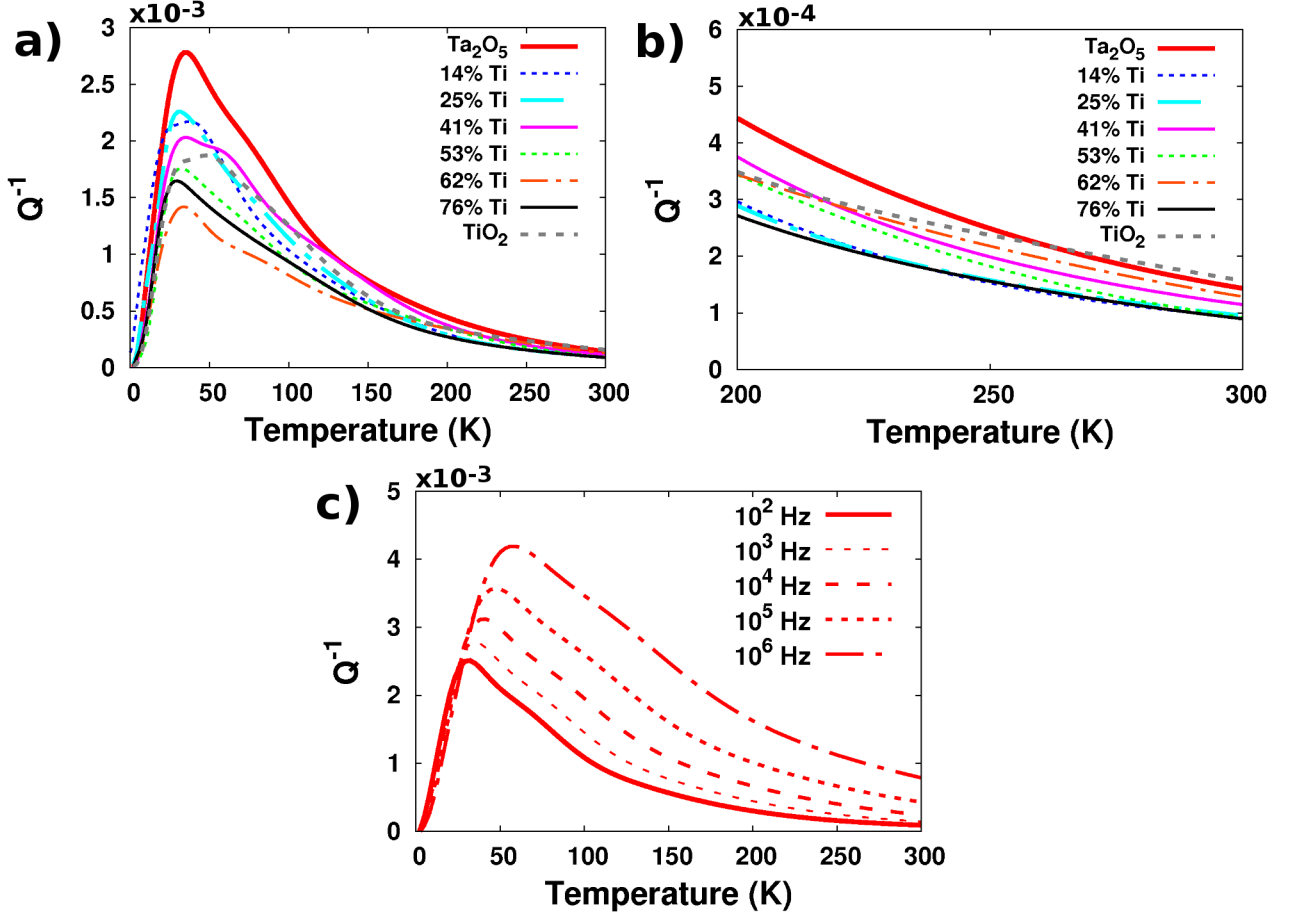
FIG. 2. Calculated internal friction (Q^{-1}) of pure and titania (TiO_2) - doped tantala (Ta_2O_5) as a function of temperature (T) and observation frequency (ω). a) $Q^{-1}(T)$ as a function of percent cation Ti doping from 0 to 300 K with $\omega = 1$ kilohertz (kHz). b) $Q^{-1}(T)$ as a function of percent cation Ti doping from 200 to 300 K with $\omega = 1$ kHz. c) $Q^{-1}(\omega, T)$ of pure Ta_2O_5.

11.00×10^{-4} (see Table 1 for comparisons to experiment). These results suggest that our model captures the dominant characteristics of the PEL of amorphous Ta_2O_5 that lead to this low-temperature peak, which we discuss in Section III.B. We also explore possible reasons for our larger peak magnitude when discussing physical parameters entering our model in Section III.C.

The internal friction for pure Ta_2O_5 decays at temperatures beyond 30 K, leading to a room temperature value of $Q^{-1}(300 \text{ K}) = 1.43 \times 10^{-4}$ (Figure 2(b)). This is on the same order of magnitude as experimental values ($Q_{exp}^{-1}(300 \text{ K}) = 2.75 \times 10^{-4}$), a factor of two smaller because our model does not a predict a plateau in Q^{-1} observed experimentally

10

beyond 200 K[9]. The atomic configurations modeled in the present study represent bulk samples with perfect stoichiometry, whereas experimental samples are frequently thin films with an often unknown stoichiometry. Either of these factors could feasibly lead to larger barrier heights that weight the distribution at higher eneries to produce such a plateau near room temperature. Therefore, we are currently studying how surfaces and stoichiometry affect the barrier distribution and resulting internal friction to understand if either is responsible for discrepancies between model and experiment. Nevertheless, this is the first model to match the order of magnitude of loss at low and room temperature in tantala and indicates that we are capturing the dominant loss mechanisms also seen in experiment. The current findings also provide an important baseline describing the characteristics of Q^{-1} due to bulk effects with which future studies of thin films and defects can be compared.

Figure 2(c) plots $Q^{-1}(\omega, T)$ of pure Ta_2O_5 as a function of temperature and observation frequency. As frequency increases, the peak consistently moves to higher temperatures and larger magnitudes. The relative changes in peak magnitude agree well with experiment, as our model predicts an approximately 10% increase in $Q^{-1}(T_{peak})$ from 100 to 1000 Hz, matching an approximately 14% increase in the experimentally measured peak for a similar increase in frequency[9]. Similar behavior is seen for all levels of Ti doping (not shown).

TABLE I. Calculated and experimental values of the peak temperature (T_{peak}), internal friction at peak temperature ($Q^{-1}(T_{peak})$), and the percent reduction of $Q^{-1}(T_{peak})$ for each Ti doping compared to pure Ta_2O_5. Experimental values are included in parentheses.

% Ti	T_{peak} (K)	$Q^{-1}(T_{peak})$ ($\times 10^{-4}$)	% reduction
0	30	27.80 (11.0)[9]	–
14	38	21.11 (8.5)[9]	24 (19)[9]
25	32	22.57	20 (32)[34]
41	35	20.31	27
53	32	17.59 (6.00)[34]	37 (46)[34]
62	34	15.78	43
76	30	16.47 (0.80)[34]	41
100	46	18.70	33

Doping Ta_2O_5 with TiO_2 consistently decreases the magnitude of the low-temperature

peak (Figure 2(a)). For the 14% Ti-doped sample, $Q^{-1}(T_{peak})$ decreases from 27.80×10^{-4} to 21.11×10^{-4}. Although our raw values are larger than those in experiment, this decrease with small Ti doping corresponds to a 24% loss reduction, matching well with the 19% reduction reported by experiment for the same level of Ti doping[9]. The internal friction at low temperature continues to decrease with further Ti doping, leading to $Q^{-1}(T_{peak}) = 17.59 \times 10^{-4}$ for 53% cation Ti doping, a 37% reduction compared to pure Ta_2O_5 that matches very well with a 46% reduction seen experimentally for the same doping level[34]. Qualitatively, moderate Ti doping broadens the low-temperature peak, with the effect most pronounced for 41% cation Ti doping. A similar feature is observed in experimental data for 14% and 55% Ti-doped samples[34]. The position of the low-temperature peak does not significantly change with Ti doping, varying between 30-38 K across all Ti doping levels. In contrast, the peak significantly shifts to higher temperature near 46 K for the pure TiO_2 sample.

Overall, our model predicts that doping Ta_2O_5 with 62% cation Ti doping minimizes the internal friction at the low-temperature peak, $Q^{-1}(T_{peak}) = 15.78 \times 10^{-4}$. This value is an order of magnitude higher compared to experimental results for a similar 76% doping level, $Q^{-1}_{exp}(T_{peak}) = 0.80 \times 10^{-4}$ (Table 1)[34]. This anomalously low experimental measurement is believed to be due to crystallization of the sample. Our model results support this conclusion and indicate that a purely amorphous sample would have a much larger peak magnitude.

Doping effects show different trends near room temperature (Figure 2(b)). All levels of cation Ti doping decrease $Q^{-1}(300 \text{ K})$ compared to pure Ta_2O_5 and range between 0.87×10^{-4} and 1.20×10^{-4}, matching recent experimental evidence that 14% cation Ti doping decreases room temperature loss[9]. Pure TiO_2 shows a similar room temperature loss as Ta_2O_5, indicating a nonmonotonic dependence of loss on doping. However, no consistent pattern of loss as a function of Ti doping is seen and therefore we cannot conclude that lower or higher levels of Ti doping consistently decrease Q^{-1} at room temperature. To the best of our knowledge, no other experimental data regarding room temperature loss exists for the other levels of Ti doping, and therefore it is difficult to compare the accuracy of these results. However, the findings generally indicate that small levels of Ti doping are enough to substantially decrease loss at room temperature.

Based on these results, our model provides an excellent representation of how TiO_2 doping affects Q^{-1} at low temperatures and identifies the systematic decrease of the magnitude

of the internal friction with TiO_2 doping. Examination of the underlying distributions (3.2), parameters (3.3), and characteristics of dominant transitions (3.4) will provide understanding of the physical processes leading to these results.

B. Barrier and Asymmetry Distributions

The underlying PEL and double well distribution of each amorphous sample dictates the temperature dependence of $Q^{-1}(\omega, T)$. Thus, to understand why Ti doping decreases the internal friction and pure titania shows a shift in $Q^{-1}(T_{peak})$, we next examine how the barrier and asymmetry distributions ($g(V)$ and $f(\Delta)$) change with increased doping levels.

Figures 3(a)-(e) plot $g(V)$ (black curve) and $\log(g)$ (red, dotted curve) for pure Ta_2O_5 and several representative Ti doping levels. The logarithm of the distribution is useful to examine because it reveals whether a more complex, multiexponential function is necessary to describe the decay of $g(V)$. Other than minor variations within small energy ranges, all barrier distributions demonstrate a generally monoexponential decay. Previous experimental studies have approximated $g(V)$ as a monoexponential function to explain experimental results[9,22], and the current findings indicate that this approximation is generally valid for tantala and titania samples.

To illustrate the major effects of TiO_2 doping on the barrier distribution, we plot $g(V)$ for pure Ta_2O_5 and several doping levels together in Figure 3(f). Ta_2O_5 exhibits a distinct peak in the distribution with the largest number of barriers occurring near 25-35 meV. The number of low-energy barriers in this range systematically decreases with Ti doping (left black arrow in Figure 3(f)). These results match experimental findings in which the barrier distribution $g(V)$ was determined by assuming a constant asymmetry distribution and fitting internal friction measurements to Equation 1[9]. This fitting procedure predicted that Ta_2O_5 exhibits a peak in $g(V)$ near 20 meV and Ti doping broadens and decreases the magnitude of the peak. Our calculated results match both of these trends, again confirming that our model is accurately capturing the major characteristics of the underlying PEL.

The second major change with Ti doping occurs for higher-energy barriers, as noted by the two right black arrows in Figure 3(f), where Ti doping increases the number of barriers between 80-110 meV and 150-200 meV. The increase in barriers in these regions are especially apparent for the pure TiO_2 sample.

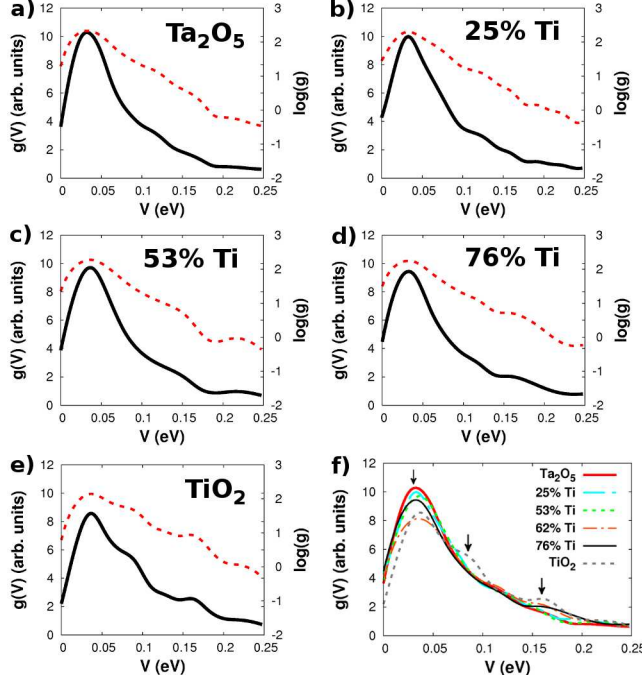FIG. 3. Normalized barrier distributions ($g(V)$) for amorphous tantala (Ta_2O_5) and various levels of cation titanium (Ti) doping. a) through e) plot $g(V)$ (black solid line) and $\log(g(V))$ (dotted red line) for pure Ta_2O_5, 25% Ti, 50% Ti, 75% Ti, and pure TiO_2, respectively. f) $g(V)$ for representative levels of Ti doping to compare and highlight major changes in barrier distribution. Black arrows emphasize significant effects of Ti doping that are discussed in more detail in the text.

To understand the impact of these trends in $g(V)$ on the internal friction, we must first determine which energy ranges of barriers influence Q^{-1} at particular temperatures. By integrating Equation 1 over Δ but removing the integral over V, we arrive at an expression that describes which barriers contribute to Q^{-1} at a given temperature:

$$f(V,T) = \frac{\gamma_l^2}{Y k_B T} \int_0^\infty \frac{\omega\tau}{1+\omega^2\tau^2} \text{sech}^2\left(\frac{\Delta}{2k_B T}\right) f(\Delta)g(V)d\Delta. \tag{7}$$

Figure 4 shows $g(V)$ (black line) and $f(V,T)$ (filled colored regions) at increasing values of temperature for Ta_2O_5. At 30K, roughly corresponding to the peak of Q^{-1} for most samples, an extremely small range of barriers around the peak of $g(V)$ dominate the contribution to the internal friction (blue filled region). Since this 40 meV peak decreases in magnitude with Ti doping (Figure refbs(f)), this will lead to a corresponding decrease in the magnitude of Q^{-1} near 30K and partially explains the decrease in low-temperature loss with the addition
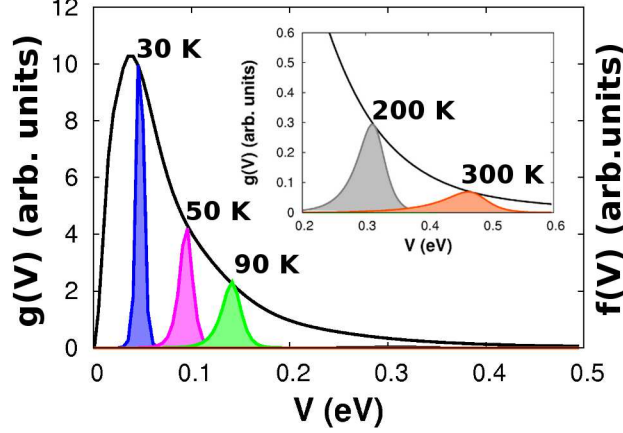
14

FIG. 4. Normalized barrier distributions ($g(V)$) for amorphous tantala (Ta_2O_5) and the expression for Q^{-1} integrated over the asymmetry distribution ($f(V,T)$) for several sample temperatures. Note the arbitrary units of both distributions, as the primary focus of this graph is to locate the energy range covered by $f(V,T)$ for a given temperature.

of Ti.

As the temperature increases, not only do higher-energy barriers dominate the contribution to Q^{-1}, but a greater spread of barriers across a larger energy range is important. Barriers just below 100 meV are most important at 50 K (purple region), which directly corresponds to the energy range of the shoulder seen in $g(V)$ for TiO_2 (Figure 3(f)). The contribution to Q^{-1} from these higher-energy barriers outweighs those near 40 meV and drives the shift in the loss peak for TiO_2 to 46 K. Since the addition of Ti atoms decreases the number of barriers near 40 meV relative to those near 100 meV, this analysis also explains the slight broadening of the loss peak to higher temperatures with Ti doping. The internal friction at 90-100 K will be dictated by barriers around 150 meV (filled green region in Figure 4), corresponding to the second region of increased barriers with Ti doping as shown in Figure 3(f). This increase in barriers with Ti doping slows the decay of Q^{-1} as a function of temperature such adding Ti atoms decreases the magnitude of Q^{-1} most significantly at low temperature.

A second intriguing discovery from this analysis is the dramatic difference in the types of transitions describing loss at different temperatures. Previous theoretical discussion of amorphous solids, usually using silica as an example, have described the loss process as transitions over low-energy barriers involving only a few oxygen rotations[35]. Our results

15

support the notion that low-energy barriers dominate the contribution to low-temperature loss. However, gravitational wave detectors and other optical devices are often concerned with room-temperature loss. As shown in Figure 4, barriers ranging between 300-550 meV dictate loss behavior at 300 K, which will likely involve significantly different structural changes compared to smaller 40 meV barriers that are important at 30 K. We explore the structural differences between these types of transitions in Section III.D to emphasize the different atomic picture necessary when discussing low-temperature and room-temperature loss.

In addition to $g(V)$, the asymmetry distribution also weights which TLSs contribute to Q^{-1}. Figures 5(a)-(d) plot $f(\Delta)/N$ for pure Ta_2O_5, 25% cation Ti, 76% cation Ti, and pure TiO_2 amorphous samples. Based on Equation 1, TLSs with $\Delta > 2k_BT$ do not significantly contribute to Q^{-1} due to the $sech^2(\Delta/2k_BT)$ term, and therefore we only plot $f(\Delta)/N < 0.06$ eV, roughly corresponding to relevant asymmetries up to 300 K. No significant differences are seen in $f(\Delta)$ across Ti dopings. In general, all amorphous samples demonstrate a slight peak at extremely small asymmetries ($\Delta < 0.01$ eV) after which the distribution is roughly flat or slightly decreasing with increasing Δ. This small peak has slightly larger values for pure Ta_2O_5 and 25% cation Ti samples, flattening out for higher levels of Ti doping. The increased frequency of low-asymmetry barriers indicates that roughly symmetric TLSs contribute more strongly to Q^{-1} than more asymmetric double wells, but that this effect will not largely change as a result of different Ti doping levels.

The present results for $f(\Delta)$ reveal details about the distribution that have been ignored in previous calculations. Previous models and experimental analyses hav often simplified the asymmetry distribution to a constant, $f(\Delta) \approx f_0$[12,16]. These assumptions have been used to fit experimental internal friction data to calculate V_0, known as the activation energy that describes the decay rate of $g(V)$[9,22,36]. The present results of a peak in $f(\Delta)$ for low asymmetries indicate that these assumptions are not always accurate. In this work, we directly input numerically calculated distributions into Equation 1 without assumptions about their shape.
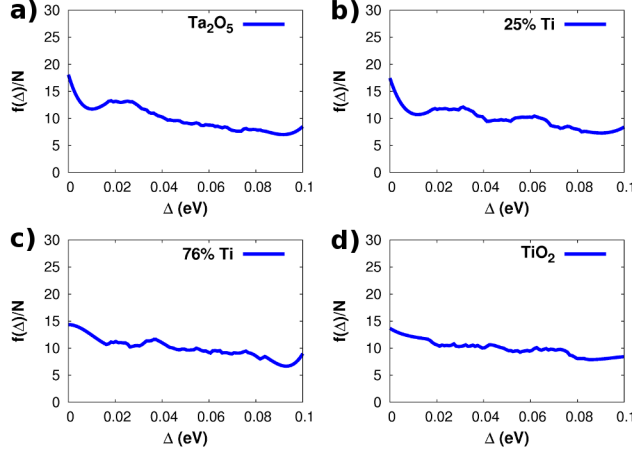
FIG. 5. Normalized asymmetry distributions ($f(\Delta)/N$) for a) amorphous tantala (Ta_2O_5), b) 25% titanium (Ti) cation doping, c) 76% Ti cation doping, and d) pure TiO_2.

C. Parameters

Beyond the barrier and asymmetry distributions, the averaged parameters included in Equation 1 have a major impact on the relative magnitude of Q^{-1} as a function of Ti doping. Figure 6 plots the relaxation time (τ_0, 6(a)), strain coupling constants (γ_l and γ_t, 6(b)), and Young's modulus (Y, 6(c)) as a function of Ti doping. In general, increased Ti doping is associated with a shorter relaxation time, smaller longitudinal coupling constant, and larger Young's modulus. Note that only the longitudinal coupling constant is used to calculate Q^{-1}, but both longitudinal and transverse components are included for comparison to future experimental measurements.

The decrease of τ_0 with Ti doping has only a small effect on the magnitude of Q^{-1}, slightly decreasing the internal friction with Ti doping, however both γ_l^2 and Y directly scale the magnitude of Q^{-1}. Since γ exhibits a squared dependence, only small changes lead to large shifts in the magnitude of Q^{-1}. As a consequence, the pattern of γ_l as a function of Ti doping generally dictates the trends in Q^{-1} at low temperature. As seen in Figure 6(b), γ_l is at a minimum for 62-76% Ti doping, matching the same doping level that minimizes the low-temperature loss peak (Figure 2(a)). In addition, shifting from a highly-doped sample to pure TiO_2 increases γ_l back to a value similar to that of pure Ta_2O_5, largely explaining the increase in $Q^{-1}(T_{peak})$ from 76%-doped Ta_2O_5 to pure TiO_2. These results suggest that substantial manipulation of the coupling constant is possible through doping and provides
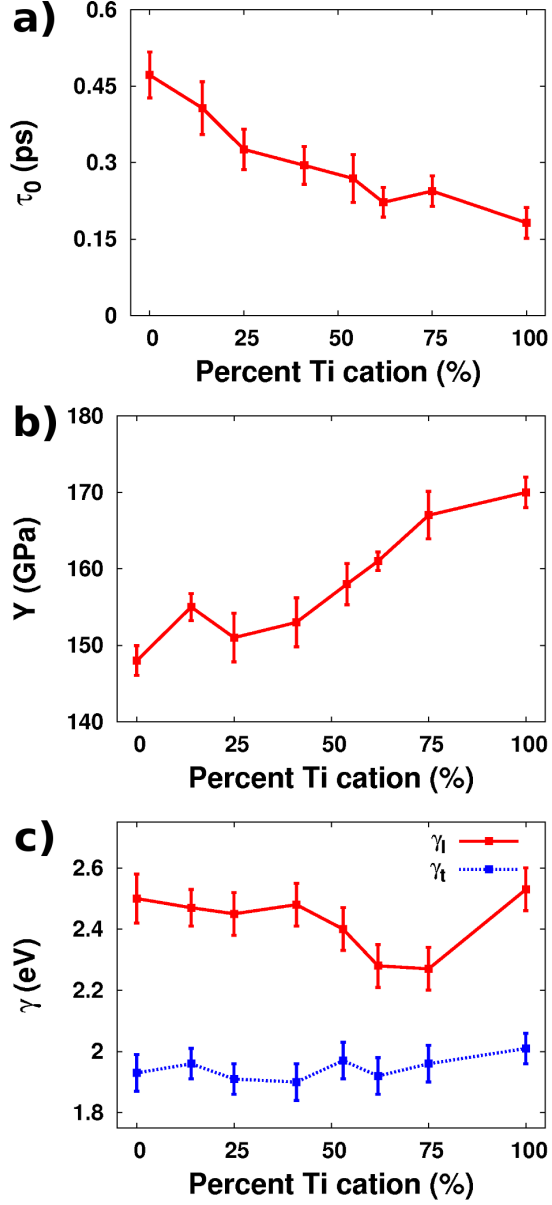
17

FIG. 6. Average values of parameters entering the numerical calculation of the internal friction (Q^{-1}). a) Relaxation time (τ_0), b) longitudinal (γ_l) and transverse (γ_t) strain coupling constant, and c) Young's modulus (Y) as a function of percent Ti cation doping.

a promising route to minimize the internal friction in these or other types of amorphous materials. The Young's modulus increases consistently with Ti doping, indicating that TiO_2 leads to a stiffer amorphous material. This also contributes to a decreased Q^{-1} with Ti doping since Y appears in the denominator of Equation 1.

As noted in Section III.A, the present calculations overestimate the magnitude of

18

$Q^{-1}(T_{peak})$ for pure and doped Ta_2O_5 compared to experiment by roughly a factor of two. One possible explanation for this may be an overestimation of the longitudinal coupling constant. Although no experimental values of either are known for Ta_2O_5, γ_t for silica has been measured as 0.9-1.0 eV and $(\gamma_l/\gamma_t)^2 = 2.25$[37]. Our calculated values of γ_l and γ_t for Ta_2O_5 are 2.5 eV and 1.95 eV, of the same order of magnitude but larger than silica's values. Thus, if we assume tantala should have a similar coupling constant as silica, our larger values can at least partially explain the overestimated low-temperature loss. However, since no previous experimental work has measured strain coupling constants in tantala, we cannot determine their accuracy. The present results clearly emphasize the parameter's importance in dictating how doping changes the magnitude of Q^{-1}. Therefore, future experimental work should attempt to measure the coupling constant in Ta_2O_5 and TiO_2 to provide benchmarks and confirm that our force fields are generating an accurate value of γ_l and γ_t.

The present results provide insight into the important physical processes that change as a result of Ti doping. In particular, the addition of TiO_2 makes the double wells of the amorphous solid less sensitive to the strain caused by the illuminating frequency, decreasing the coupling constant. This, in combination with TiO_2 increasing the stiffness of the material and increasing Y, explains the decreased magnitude of Q^{-1} observed experimentally.

D. Atomic Characterization of Two-Level Transitions

Having explained the effect of Ti doping on Q^{-1} by exploring the TLS distributions and parameters, we finally provide an atomic description of the two-level transitions dominating mechanical loss at low and room temperature. Many structural changes could play a role in typifying TLS transitions, and a comprehensive analysis of all factors predicting barrier height, asymmetry, and loss is beyond the scope of this paper. However, previous work has suggested that anion rotations around central cations are a primary characteristic of transitions in amorphous oxides[35]. Therefore, we focus on analyzing the number of atoms involved in each transition, the number and magnitude of O rotations, as well as changes in Ta/Ti-O bond length to characterize transitions in tantala and titania.

Since our previous discussion in Section III.B described how TLS barrier height connects to loss at different temperatures (Figure 4), we focus on associating structural characteristics

to different energy ranges of V. In particular, we highlight three categories: the peak of $g(V)$ (0-60 meV), the shoulder that increases for pure TiO_2 (60-120 meV), and the increase in barriers with Ti doping between 120-240 meV. TLS asymmetry is not strongly correlated with most structural characteristics (r $\approx$ 0.20) and is not discussed in detail here.

Figures 7(a)-(d) display histograms for each structural characteristic considered across all TLS and within each barrier range for Ta_2O_5 (left column) and TiO_2 (right column). Histograms for data from Ti-doped samples resemble combinations of pure tantala or titania, so here we only analyze the two extremes to identify the major changes between them. For example, data for the 25% Ti-doped Ta_2O_5 sample will largely resemble patterns in the Ta_2O_5 histograms with slight trends toward TiO_2 patterns.

As seen in Figure 7(a), most transitions in Ta_2O_5 involve around 30 atoms, with very few transitions involving more than 150 atoms. A correlation exists between the number of atoms involved and barrier height (r = 0.55 for Ta_2O_5, r = 0.44 for TiO_2), such that higher-energy barriers generally involve more atoms. For Ta_2O_5, barriers between 60-120 meV involve 30-70 atoms, and barriers between 120-240 meV are associated with a large range of 30-100 atoms. In contrast, titania shows a sharpening of the histogram peak near 30 atoms for barriers in both the 0-60 meV and 60-120 meV ranges (Figures 7(a), right column). This is evidence of a localized, higher-energy barrier between 60-120 meV that is more prominent in titania. It is this type of TLS transition that creates the shoulder in $g(V)$, leading to the broadened loss peak at higher temperature compared to tantala (Figure 2(a)).

Regarding oxygen rotations, TLS transitions in both Ta_2O_5 and TiO_2 typically involve five O atoms rotating more than 10 degrees around a central Ta atom (Figure 7(b)) with the largest rotation between 18-20 degrees (Figure 7(c)). A correlation again exists between barrier height and number of oxygen rotations (r = 0.54 for Ta_2O_5, r = 0.47 for TiO_2) and largest oxygen rotation angle (r = 0.67 for Ta_2O_5, r = 0.66 for TiO_2), such that larger barriers are associated with more O atoms being involved with larger rotation angles. Most low-energy barriers (0-60 meV) in tantala involve only 3-5 O atoms, whereas titania demonsrates a wider distribution of oxygen atoms involved. Also, compared to tantala, titania exhibits larger barriers that involve more O atoms rotating at larger angles (red bars in Figures 7(b-c)), confirming the analysis of the barrier distributions in Section III.B.

Finally, the histograms of the Ta/Ti-O bond length changes are shown in Figure 7(d).
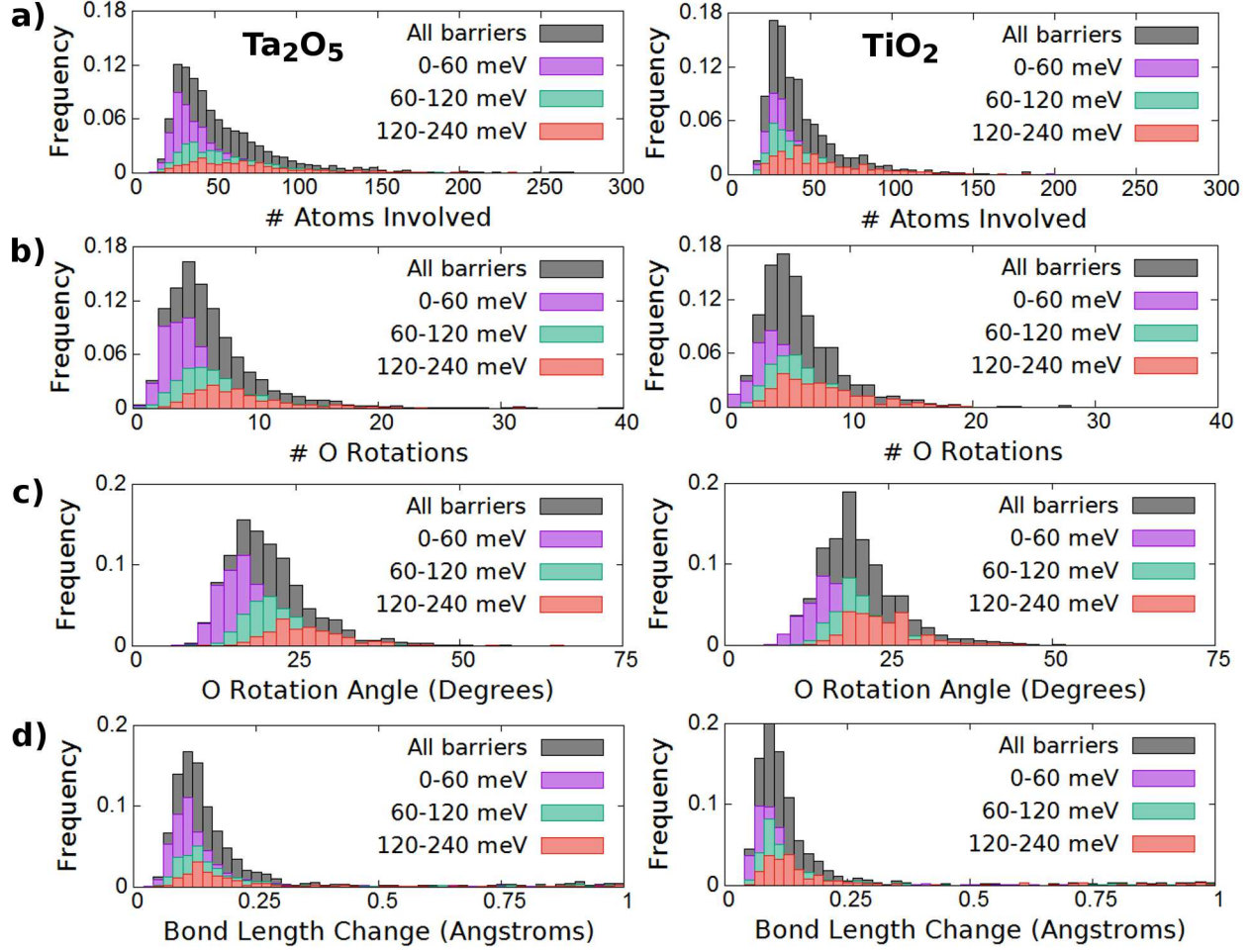
20

FIG. 7. Histograms for tantala (Ta$_2$O$_5$, left column) and titania (TiO$_2$, right column) of a) the number of atoms involved in two-level-system (TLS) transitions, b) number of O rotations greater than 10 degrees, c) largest O rotation angle, and d) largest change in Ta/Ti-O bond length. Differently colored histograms correspond to subsets of TLS transitions categorized by barrier height (V). All distributions are normalized to the total number of samples across all barrier heights. An atom is considered part of a transition if its position changes by at least 0.1 Angstrom between minima.

Both tantala and titania show very similar trends in this case, with most changes in bond length roughly between 0.12-0.16 Angstroms. A much smaller correlation associates barrier height with bond length changes (r = 0.27 for Ta$_2$O$_5$, r = 0.23 for TiO$_2$), indicating the total number of involved atoms and rotating oxygen atoms are the primary characteristics determining the barrier heights of the two-level systems.

21

This structural analysis of TLS transitions in titania and tantala reveal that, despite small differences, the two amorphous oxides support very similar loss mechanisms. Differences between histograms in Figure 7 only involve slight shifts in the typical number atoms involved or size of oxygen rotation angles, as discussed above, but transitions in the two amorphous oxides generally share similar structural traits. These findings indicate that the oxides match well in the sense that doping one with the other will not qualitatively change the loss behavior, a conclusion confirmed by the same low-temperature peak in Q^{-1} across all Ti dopings followed by decay with increasing temperature. Instead of distinctly different types of structural transitions, our analyses reveal that TiO_2 differs from Ta_2O_5 by allowing more high-energy transitions with barriers between 60-240 meV. It is this difference in barrier frequency that leads to the shift in the low-temperature peak to 46 K for TiO_2.

To provide a final perspective on the two-level systems driving mechanical loss, Figure 8 visualizes three typical transitions in Ta_2O_5 and TiO_2 that highlight the differences between low and room temperature as well as the prototypical transition near 100 meV that occurs more frequently in TiO_2. The left column of the figure shows the first minimum in the TLS (blue cations and red anions), the right column shows the second minimum (green cations and brown anions), and the middle column visualizes their overlap to emphasize the major changes between them. Atoms not involved in the transition are displayed as faint grey octahedra in the background.

In Figure 8(a), we illustrate a typical pair of minima from a TLS that drives the 30 K loss peak in Ta_2O_5. This type of transition has a barrier height of 32 meV, involves 30 atoms, four O rotations above 10 degrees, and spans about 8 Angstroms. Two, 20-degree oxygen rotations, identified by the black arrows, appear to drive the transition, causing smaller deformations rippling away from these central atoms. In contrast, Figure 8(b) shows a typical transition dominating room temperature loss. This transition has a barrier of 453 meV, involves 149 atoms, 10 O rotations over 10 degrees, and spans 20 Angstroms. This type of transition cannot be localized to the motion of one or two primary oxygen atoms, as was described for the low-temperature transition, but rather includes a multitude of rotations spread across the supercell.

Finally, Figure 8(c) represents a typical transition leading to the increase in $g(V)$ near 100 meV for pure titania. Compared to the TLS with a low-energy barrier shown in Figure 8(a), this transition is slightly less localized, with 35 atoms moving across 10 Angstroms, and
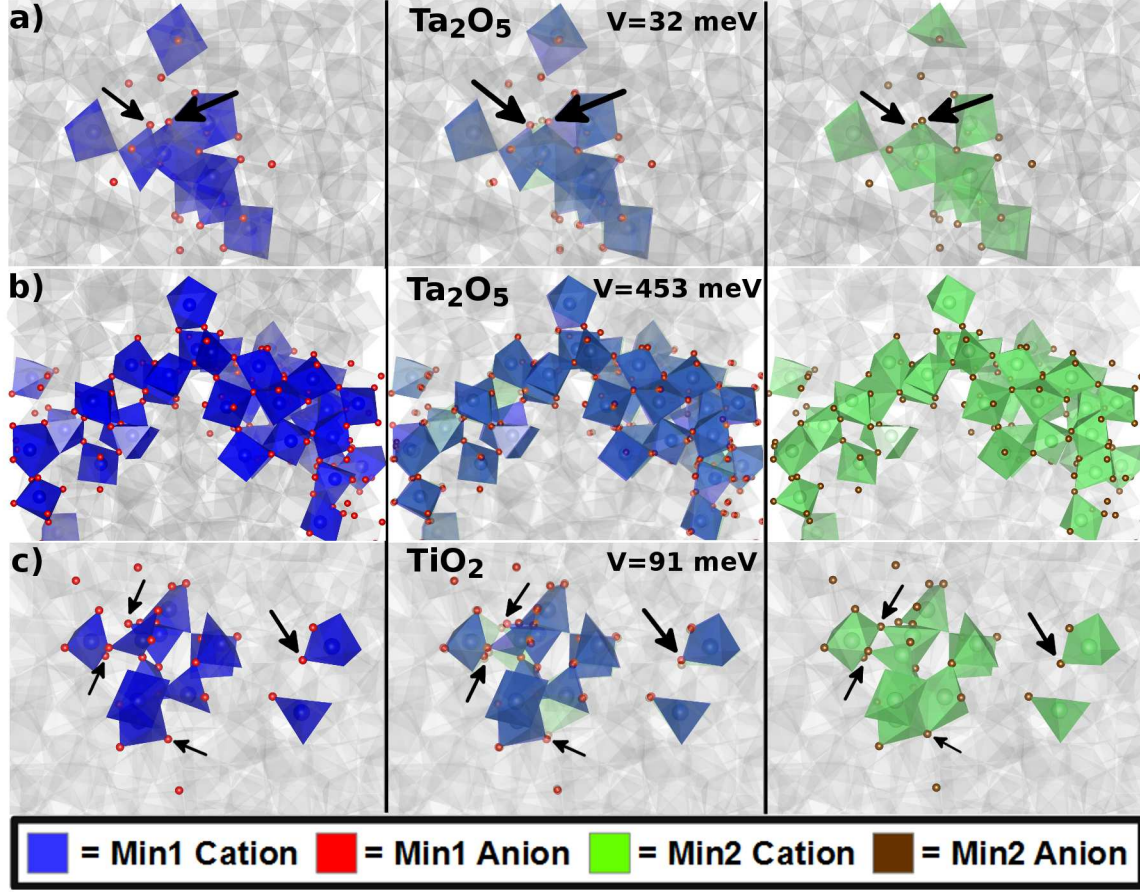
FIG. 8. Configurations of local minima for three sample two-level systems (TLS) for a) tantala (Ta_2O_5) ($V = 32$ meV), b) Ta_2O_5 ($V = 453$ meV), and c) TiO_2 ($V = 91$ meV). The left column shows the configuration of the first minimum in the transition, the right column shows the second minimum, and the middle column visualizes their overlap to emphasize the differences between minima. Black arrows highlight the major oxygen rotations making up each transition. Blue octahedra and red spheres represent the cation and anion of the first minimum, respectively. Green octahedra and brown spheres represent the cation and the anion of the second minimum.

involves six O rotations, with one angle over 25 degrees. As emphasized by the black arrows, four of these O rotations are over 20 degrees and are spread out across the configuration, in contrast to the two localized rotations shown in Figure 8(a). This result indicates that titania supports transitions that are still described by only a few oxygen rotations but that are spread out to a greater degree compared to tantala.

This atomic description of TLS transitions with small and larger barriers is necessary to consider when predicting which types of dopants will minimize loss. To decrease Q^{-1}, one

must identify a dopant that blocks the typical transition providing the most thermal noise. However, these results indicate that the dominant transition type varies dramatically with temperature, suggesting that dopants must also be selected to prevent motion characteristic at either low or high temperature. Using Ta_2O_5 and TiO_2 as an example, adding Ti decreases the number of low-energy barriers characterized in Figure 8(a) in favor of the type seen in Figure 8(c). This change in localized transitions influences the barrier distribution between 0-150 meV, impacting low-temperature loss most significantly. However, these transitions have little impact on room temperature loss. To affect Q^{-1} at 300 K, doping combinations must be chosen that affect large-scale configurational changes similar to that exemplified in Figure 8(b). To the best of our knowledge, this distinction has not been discussed in the literature before and should be emphasized in future discussions of minimizing loss with dopants.

IV.   CONCLUSIONS

We have combined molecular dynamics (MD) simulations with numerical techniques to calculate the internal friction (Q^{-1}) for pure and titania-doped tantala. Strain from a perturbing sound wave induces energy dissipation in amorphous solids that we have modeled as thermally activated transitions between two-level systems. Applying the interval bisection and nonlocal ridge methods within MD simulations, we have calculated the barrier $(g(V))$ and asymmetry $(f(\Delta))$ distributions describing the ensemble of two-level systems for each amorphous sample. From these distributions, we have computed $Q^{-1}(\omega, T)$ for pure and doped tantala. By connecting loss behavior at certain temperatures with certain types of TLS transitions, we provide the first atomic description of the configurational changes dominating loss at low and room temperatures.

The results from our model reproduce the low-temperature peak in Q^{-1} between 20-30 K seen in experimental measurements of pure and doped tantala. The magnitude of the calculated peak for pure Ta_2O_5 is within a factor of 2-3 of experiment, suggesting that our model has captured the dominant transitions between two-level systems that lead to this signature characteristic. Increasing Ti content consistently decreases Q^{-1} at low temperature due to a broadening of the barrier distribution to higher energies, an increasing Young's modulus, and a decreasing longitudinal coupling constant with doping. We find that 62%

cation Ti doping minimizes the magnitude of the internal friction peak. Doping Ta_2O_5 with 14% cation Ti and 53% cation Ti lead to 24% and 37% reductions in the peak magnitude of Q^{-1}, respectively, both of which agree well with experimental findings for the same doping levels and confirm the accuracy of the theory and interatomic force fields used.

The ability to calculate the mechanical loss with atomic resolution has provided several key findings to inform future experiment and design of optimal doping combinations. First, tantala and titania have very similar barrier distributions, differentiated only by a decrease in the 30 meV peak with Ti doping and corresponding increase in barriers near 100 and 200 meV. This change in the distribution leads to the low temperature loss peak decreasing and broadening slightly due to less low-energy barriers being available when Ti is added as a dopant. However, our results support the idea that tantala and titania are congruent dopants and have the same qualitative, low-temperature loss peak. Because of this, changes in the TLS distribution only change the magnitude of the loss peak as a function of Ti doping, not its general shape.

Second, the coupling constant is the primary parameter dictating the magnitude of the low temperature loss peak. This quantity describes the sensitivity of the TLS asymmetry to an applied strain. Very little experimental research has considered this parameter when discussing how doping affects mechanical loss. Our results encourage experimental measurements of this quantity in tantala and titania samples using fitting to low-temperature models, since our findings reveal that controlling the coupling constant could be an effective way to minimize loss.

Third, this is the first study to provide an atomic glimpse of the transitions characterizing mechanical loss at low and room temperature. On average, transitions in tantala contributing to loss at low temperature (V=30-40 meV) involve 30 atoms and four oxygen rotations with angles greater than 10 degrees. Structural changes in these transitions appear well-localized around 1-2 rotations of 15-20 degrees, with smaller rotations radiating out roughly 8 Angstroms and involving 8-10 cation octahedra. The substitution of Ti cations to tantala leads to a higher frequency of more delocalized transitions ($V = 80-110$ meV) that involve several oxygen rotations over 20 degrees spread across 10 Angstroms, driving loss near 40-50 K.

In contrast to this low temperature behavior, TLS transitions dictating loss at room temperature look qualitatively different. These transitions (V=350-550 meV) involve an average

of 130 atoms diffusely spread across 20 Angstroms and 16 oxygen rotations, with multiple rotations above 25 degrees. Thus, the simplistic picture of one or two anion rotations first exemplified in silica does not apply to room temperature loss mechanisms. This is important information when considering how to decrease loss, as dopants must be chosen to block specific atomic motion that characterizes the internal friction at a particular temperature.

The largest discrepancies between our model and experimental data occur near room temperature, where experimental data demonstrate a plateau in Q^{-1} for temperatures above 200 K. In contrast, our results suggest a continually decreasing mechanical loss with temperature, due to the decreasing frequency of high-energy barriers, that leads to an underestimation of Q^{-1} near 300 K. The reasons for this discrepancy are likely due to differences between our modeled samples and those used in experiment. In particular, we have only examined bulk, perfectly stoichiometric samples, whereas experimental measurements have been taken on thin films that may feature strong surface effects and non-stoichiometric defects. For example, in silica, experimental bulk and thin film samples have revealed differences in the decay of the barrier distribution, and it is likely that amorphous tantala and titania would show similar behavior. Thus, future work is currently underway to understand how surface effects and stoichiometry affect the temperature dependence and magnitude of the internal friction. In addition, the interatomic potential used in the present study may not be correctly describing medium-range or long-range order that could affect the internal friction at higher temperature. The potentials used were fitted to experimental radial distribution functions with a particular focus on matching the first bonding shell. We are currently working with experimentalists to compare the medium-range structure seen experimentally with our model predictions and improve the interatomic potentials as necessary to model this longer-range structure.

Despite these limitations, this is the first study using computational modeling of tantala and titania with atomic resolution that matches the characteristic low-temperature loss behavior seen consistently in experiment. We have identified the primary differences between the TLS distributions in tantala and titania that drive changes in loss behavior. Our insights into the atomic configurations making up TLS transitions reveal the types of atomic motion that contribute to the internal friction and low and room temperature. These findings are the first look into the microscopic processes guiding mechanical loss in tantala and titania and provide an important benchmark with which to compare future studies of doping

combinations, surface effects, and non-stiochiometric samples.

ACKNOWLEDGMENTS

---

[1] Y. Jiang, A. Ludlow, N. Lemke, R. Fox, J. Sherman, L.-S. Ma, and C. Oates, Nature Photonics **5**, 158 (2011).

[2] G. M. Harry, A. M. Gretarsson, P. R. Saulson, S. E. Kittelberger, S. D. Penn, W. J. Startin, S. Rowan, M. M. Fejer, D. R. M. Crooks, G. Cagnoli, J. Hough, and N. Nakagawa, Classical and Quantum Gravity **19**, 897 (2002).

[3] P. R. Saulson, Phys. Rev. D **42**, 2437 (1990).

[4] R. Bassiri, K. Evans, K. Borisenko, M. Fejer, J. Hough, I. MacLaren, I. Martin, R. Route, and S. Rowan, Acta Materialia **61**, 1070 (2013).

[5] A. V. Cumming, K. Craig, I. W. Martin, R. Bassiri, L. Cunningham, M. M. Fejer, J. S. Harris, K. Haughian, D. Heinert, B. Lantz, A. C. Lin, A. S. Markosyan, R. Nawrodt, R. Route, and S. Rowan, Classical and Quantum Gravity **32**, 035002 (2015).

[6] G. M. Harry, M. R. Abernathy, A. E. Becerra-Toledo, H. Armandula, E. Black, K. Dooley, M. Eichenfield, C. Nwabugwu, A. Villar, D. R. M. Crooks, G. Cagnoli, J. Hough, C. R. How, I. MacLaren, P. Murray, S. Reid, S. Rowan, P. H. Sneddon, M. M. Fejer, R. Route, S. D. Penn, P. Ganau, J.-M. Mackowski, C. Michel, L. Pinard, and A. Remillieux, Classical and Quantum Gravity **24**, 405 (2007).

[7] S. D. Penn, P. H. Sneddon, H. Armandula, J. C. Betzwieser, G. Cagnoli, J. Camp, D. R. M. Crooks, M. M. Fejer, A. M. Gretarsson, G. M. Harry, J. Hough, S. E. Kittelberger, M. J. Mortonson, R. Route, S. Rowan, and C. C. Vassiliou, Classical and Quantum Gravity **20**, 2917 (2003).

[8] D. R. M. Crooks, G. Cagnoli, M. M. Fejer, G. Harry, J. Hough, B. T. Khuri-Yakub, S. Penn, R. Route, S. Rowan, P. H. Sneddon, I. O. Wygant, and G. G. Yaralioglu, Classical and Quantum Gravity **23**, 4953 (2006).

⁹ I. Martin, E. Chalkley, R. Nawrodt, H. Armandula, R. Bassiri, C. Comtet, M. Fejer, A. Gretarsson, G. Harry, D. Heinert, *et al.*, Classical and Quantum Gravity **26**, 155012 (2009).

¹⁰ R. F. Greene and H. B. Callen, Physical Review **88**, 1387 (1952).

¹¹ N. Theodorakopoulos and J. Jäckle, Physical Review B **14**, 2637 (1976).

¹² W. Phillips, Journal of Low Temperature Physics **7**, 351 (1972).

¹³ P. W. Anderson, B. I. Halperin, and C. M. Varma, Philosophical Magazine **25**, 1 (1972).

¹⁴ R. Zeller and R. Pohl, Phys. Rev. B **4**, 2029 (1971).

¹⁵ J. Jäckle, Zeitschrift für Physik **257**, 212 (1972).

¹⁶ K. S. Gilroy and W. A. Phillips, Philosophical Magazine Part B **43**, 735 (1981).

¹⁷ K. Topp and D. G. Cahill, Zeitschrift für Physik B Condensed Matter **101**, 235 (1996).

¹⁸ A. Heuer and R. J. Silbey, Phys. Rev. B **49**, 1441 (1994).

¹⁹ J. Reinisch and A. Heuer, Phys. Rev. B **70**, 064201 (2004).

²⁰ B. Doliwa and A. Heuer, Phys. Rev. E **67**, 031506 (2003).

²¹ R. Hamdan, J. P. Trinastic, and H. P. Cheng, The Journal of Chemical Physics **141**, 054501 (2014).

²² I. Martin, H. Armandula, C. Comtet, M. Fejer, A. Gretarsson, G. Harry, J. Hough, J. M. Mackowski, I. MacLaren, C. Michel, *et al.*, Classical and Quantum gravity **25**, 055005 (2008).

²³ G. Henkelman, B. P. Uberuaga, and H. Jnsson, The Journal of Chemical Physics **113**, 9901 (2000).

²⁴ W. Kauzmann, Rev. Mod. Phys. **14**, 12 (1942).

²⁵ D. Tielbürger, R. Merz, R. Ehrenfels, and S. Hunklinger, Phys. Rev. B **45**, 2750 (1992).

²⁶ Y.-N. Wu, L. Li, and H.-P. Cheng, Phys. Rev. B **83**, 144105 (2011).

²⁷ J. P. Trinastic, R. Hamdan, Y. Wu, L. Zhang, and H.-P. Cheng, The Journal of Chemical Physics **139**, 154506 (2013).

²⁸ W. Smith and T. Forester, Journal of Molecular Graphics **14**, 136 (1996).

²⁹ B. W. H. van Beest, G. J. Kramer, and R. A. van Santen, Phys. Rev. Lett. **64**, 1955 (1990).

³⁰ O. Anderson, C. R. Ottermann, R. Kuschnereit, P. Hess, and K. Bange, Fresenius' Journal of Analytical Chemistry **358**, 290 (1997).

³¹ O. Zywitzki, T. Modes, H. Sahm, P. Frach, K. Goedicke, and D. Glob, Surface and Coatings Technology **180**, 538 (2004), proceedings of Symposium G on Protective Coatings and Thin Films-03, of the E-MRS 2003 Spring Conference.

[32] V. Petkov, G. Holzhuter, U. Troge, T. Gerber, and B. Himmel, Journal of Non-Crystalline Solids **231**, 17 (1998).

[33] J. Horbach and W. Kob, Phys. Rev. B **60**, 3169 (1999).

[34] I. Martin, K. Craig, P. Murray, R. Robie, S. Reid, A. Cumming, R. Bassiri, M. Fejer, J. Harris, M. Hart, *et al.*, GWADW, Takayama, May (2014).

[35] W. Phillips, Reports on Progress in Physics **50**, 1657 (1987).

[36] I. Martin, R. Nawrodt, K. Craig, C. Schwarz, R. Bassiri, G. Harry, J. Hough, S. Penn, S. Reid, R. Robie, *et al.*, Classical and Quantum Gravity **31**, 035019 (2014).

[37] J. Van Cleve, A. Raychaudhuri, and R. Pohl, Zeitschrift für Physik B Condensed Matter **93**, 479 (1994).